Use of a Toroidal Nozzle for Welding Duplex Stainless Steel

Tomasz Giętka[1], Małgorzata Trepczyńska-Łent[2*]

[1] OLTECH, Witebska 1, 85-759 Bydgoszcz, Poland

[2] Department of Mechanical Engineering, Bydgoszcz University of Science and Technology, Aleja prof. S. Kaliskiego 7, 85-796 Bydgoszcz, Poland

* Corresponding author's e-mail: malgorzata.trepczynska-lent@pbs.edu.pl

ABSTRACT

The goal of this research was to determine the appropriate parameters for welding two-phase duplex stainless steel (DSS) and to understand the challenges involved in the process. For welding pipes with diameters of ø25 mm and ø38 mm of steel type 1.4462, the classic tungsten inert gas (TIG) method and TIG with a toroidal shielding gas nozzle were used. The aim was to improve the durability and service life of welded joints produced using the toroidal shielding gas nozzle compared to those produced using traditional TIG methods for DSS welding. The welding process was carried out using the parameters: arc voltage 9V, welding current 105A for TIG and 80A with a toroidal shielding gas, welding speed 90 mm/min for TIG and 95 mm/min with a toroidal shielding gas. The welded elements were tested for quality properties. Tests such as visual, penetration, radiographic, and destructive tests (macroscopic, ferrite content, hardness, microscopic, diffraction, static strength, and fatigue) were conducted on the test samples prepared in the TIG process. The actual test results were compared to the acceptable values from the standards. Using a toroidal nozzle in the welding process had lowered the ferrite content in the surface layers by about 10% in comparison to the traditional TIG method. The morphology and phase arrangement of the tested welded joints varied significantly, even when utilizing a toroidal nozzle. The analysis of the determined durability showed that welding with a toroidal shielding gas nozzle provided superior results, with enhancements ranging from 4% to 132%. Furthermore, the use of a toroidal nozzle reduced gas consumption by 17% for each joint type compared to conventional welding. In terms of service life, the joints welded with a toroidal nozzle demonstrated nearly twice the longevity of those welded with traditional methods.

Keywords: TIG process, duplex stainless steel, toroidal shielding gas nozzle, non-destructive testing, destructive testing.

INTRODUCTION

Steel must be able to be welded without significant limitations in order to be widely adopted. Contemporary duplex stainless steel grades meet this requirement, with some variations between different grades [1–3]. The duplex stainless-steel family has been expanded in recent years to include new lean grades and highly-alloyed hyperduplex grades. While welding recommendations for duplex stainless steel have not changed much since 1990's, the introduction of new grades and the use of newer welding methods have changed perceptions of what is possible [4–6]. DSS have a combination of strong mechanical properties and high corrosion resistance. The effect of microstructure on the mechanical properties and corrosion resistance of duplex stainless steel has been demonstrated [7–9]. The duplex steel's two-phase structure and increased nitrogen content (0.3–0.5%) results in almost double the strength compared to traditional austenitic steels. It also contributes to the faster formation of austenite during welding. The duplex steel's two-phase structure conditions a low tendency for hot cracking and increased corrosion resistance. Grain growth in the heat-affected zone (HAZ) is significantly limited. Duplex steel welding can be carried out using all welding methods used for joining austenitic steels. Mentioning the shortcomings of duplex steel, it

should be mentioned about the tendency to form a brittle sigma σ phase (475 °C) in the HAZ. This can be avoided by regulating the cooling rate. The ferrite content in the weld should be in the range of 22 to 70%. During TIG welding, it is recommended to introduce nitrogen N_2 into the shielding and forming gas composition. The welding speed with this method is slightly lower than when joining austenitic steels [10–12].

However, some concerns exist about the effects of welding on the microstructure and properties in the HAZ. For example, the best corrosion resistance is often achieved when the ferrite and austenite contents are roughly equal. When improperly welded, duplex stainless steels are at a high risk of forming harmful intermetallic phases, which can cause severe structural failures. Compared to stainless steels (SS), DSS exhibit greater resistance to stress corrosion cracking (SCC) than austenitic SS, though they are less resistant than ferritic SS. Additionally, DSS generally have better toughness than ferritic SS but do not match the toughness of austenitic SS. DSS are characterized by their dual-phase microstructure, consisting of approximately equal parts of ferrite (α-phase) and austenite (γ-phase). It is well-established that the best corrosion resistance and mechanical properties in a DSS weldment are achieved with a 50:50 balance of ferrite to austenite. However, attaining this precise balance in weldments is challenging due to various factors such as metal composition, welding techniques, and the thermal history of the steel. Research and practical experience have shown that maintaining a ferrite content between 35% and 60% in the weldment results in optimal corrosion resistance and mechanical properties [12, 13].

If improper welding procedures are used, issues such as a high ferrite content or the formation of nitrides and intermetallic phases can occur [14, 15]. Conversely, if the cooling rate is too slow or if there is repeated heating in multipass welding or repair welding, intermetallic phases can form. Even a small amount of sigma phase can greatly reduce the impact toughness [16–18].

The control of ferrite and austenite phase balance is crucial in the welding of duplex stainless steels. This balance can be achieved through the use of appropriate filler materials, the addition of nitrogen to the shielding gas, the regulation of heat input, post-weld heat treatment, and the application of an alternating magnetic field. Excessive cooling rates lead to the formation of additional ferrite and chromium nitride precipitation.

Conversely, insufficient cooling rates or repeated heating cause the precipitation of secondary austenite and intermetallic compounds. Both scenarios negatively impact the mechanical properties and corrosion resistance of DSS welds. Therefore, it is essential to adhere to the recommended upper and lower limits for heat input and the maximum interpass temperature [19].

Duplex stainless steels offer numerous advantages due to their unique combination of austenite and ferrite grains. They are essential for modern applications, providing superior corrosion resistance compared to widely used austenitic stainless steels. This paper examines the weldability of DSS, explaining the reasons for their necessity and tracing their development. It covers the phase transformations in the heat-affected zones during DSS welding, with detailed analysis of the formation, microstructure, and changes in both high and low-temperature HAZ. The influence of cooling rates on austenite formation is also discussed. Additionally, the paper compares the weldability of austenitic and duplex stainless steels. Lastly, it reviews the applications of various DSS grades across industries such as chemical processing, paper manufacturing, and power generation, and explores the future potential of DSS in various industrial sectors [20].

The microstructure, elemental distribution, and pitting corrosion resistance of gas tungsten arc welding (GTAW) duplex stainless steel joints using 100% argon (Ar) and a 98% Ar + 2% nitrogen (N_2) shielding gas mixture were analyzed with optical microscopy, scanning electron microscopy, energy dispersive spectroscopy, and electrochemical corrosion testing. The results indicate that adding N_2 to the shielding gas enhances the formation of the austenite (γ) phase in the weld joint. The austenite phase exhibits a dendritic distribution, and the ferrite (δ) and austenite phases in the heat-affected zone no longer form banded structures. Additionally, the austenite phase in the weld is enriched with nickel (Ni) and nitrogen (N), whereas the ferrite phase is enriched with chromium (Cr) and molybdenum (Mo). The pitting resistance equivalent number (PREN) at the austenite/ferrite (δ/α) phase boundary is lower than that of the δ and γ phases, making it more susceptible to corrosion. The presence of chromium nitride (Cr_2N) reduces the corrosion resistance of the weld and heat-affected zone. However, N_2 in the 98% Ar + 2% N_2 shielding gas can inhibit Cr_2N precipitation, increase the PREN of the secondary

austenite structure (γ2), and enhance the pitting corrosion resistance of the welded joints [21].

In this study, S32101 duplex stainless steel welded joints were produced using a K-TIG welding system. The weld geometry parameters at different welding speeds were analyzed in conjunction with the morphological characteristics of the keyhole. The microstructure and impact toughness of both the base metal and weld metal zone under various welding speeds were examined. The results indicate that welding speed significantly influences the weld geometry profile. Furthermore, the keyhole's characteristic parameters can effectively predict the weld geometry profile. The findings demonstrate that the microstructure, $\Sigma3$ coincidence site lattice grain boundary, and the phase boundary between ferrite and austenite impact the weld metal zone's toughness. An increase in the proportion of austenite, $\Sigma3$ coincidence site lattice grain boundaries, and random phase boundaries correlates with enhanced impact toughness of the weld metal zone [22].

Efficient and accurate welding technologies, including several high-energy density beam welding techniques, are typically employed for welding mid-thick duplex stainless steel. However, issues such as blowholes, excessive ferrite content, and coarse columnar grains remain unresolved. In this study, the keyhole gas tungsten arc welding technique, a novel process, was utilized. The microstructural characterization, hardness, and pitting corrosion of weld metal (WM) under different heat inputs were thoroughly investigated. The results indicate that appropriate welding parameters can effectively prevent weld defects. As heat input increases, Widmanstätten austenite content rises while fine-grained intergranular austenite (IGA) content decreases. The hardness of the austenite in the WM is influenced by nitrogen solubility and dislocation proliferation caused by deformation. Additionally, the PREN of ferrite in the WM is lower than that of austenite. Despite similar chemical compositions, the corrosion rate of WM increases with higher heat inputs. The initiation and propagation of pits are significantly affected by precipitated Cr_2N, PREN, and $\Sigma3$ coincident site lattice boundaries. Moreover, fine-grained IGA improves the stability and continuity of the passive film [23].

The microstructure, mechanical, and corrosion properties of dissimilar activated tungsten inert gas (ATIG) welded 2205 duplex stainless steel (2205 DSS) and AISI 316L austenitic stainless steel (316L ASS) plates were compared to conventional tungsten inert gas welds. The mixing design method was employed to determine the optimal combined flux for achieving a fully penetrated weld bead in a single pass. Microstructural analysis was conducted using scanning electron microscopy. The fusion zones of both ATIG and TIG welds exhibited matrix ferrite structures with intragranular austenite, Widmanstätten needles, allotriomorphic austenite at grain boundaries, and plate-like precipitates, free from deleterious sigma and chi phases or secondary austenite, due to moderate heat input of 0.8 kJ/mm. The ferrite volume fraction in the ATIG weld zone was 54%, compared to 47% in the TIG weld zone. Optimal flux consisting of 91% Mn_2O_3 and 9% Cr_2O_3 enabled a fully penetrated weld in a single pass, whereas conventional TIG required double-sided welding. The tensile strength (599 MPa), hardness (235 HV), and impact resistance (267 J/cm²) of ATIG welds were comparable to TIG welds, with no degradation in mechanical properties. The ATIG heat-affected zone was 2.6 times narrower than that of TIG, resulting in less joint distortion. Potentiodynamic polarization tests showed superior electrochemical behavior for 316L ASS compared to the weldment and DSS 2205 base metal [24].

In the newly developed 2101 lean duplex stainless steel, oxide inclusions were detected in welded metal zones after flux-cored arc welding with E2209T1-1 flux-cored filler metal. These oxide inclusions affect the mechanical properties of the weld metal. A proposed correlation between oxide inclusions and mechanical impact toughness was investigated using scanning electron microscopy and high-resolution transmission electron microscopy. The study found that spherical oxide inclusions comprised a mixture of oxides within the ferrite matrix, often near intragranular austenite. These inclusions were identified as titanium- and silicon-rich oxides with amorphous structures, MnO with a cubic structure, and TiO_2 with orthorhombic/tetragonal structures, originating from the deoxidation of the filler metal/electrodes. The type of oxide inclusions did not significantly affect the absorbed energy, and no crack initiation occurred near them [25].

For producing thick-walled duplex steel welded joints, X2CrNiMoN22 duplex steel in 15 mm thick plates was used. The welded joint was produced using the Hybrid Laser Arc Welding (HLAW) method, which combines laser welding

with Gas Metal Arc Welding and Submerged Arc Welding (SAW). The HLAW method was used for the root pass, while the SAW method was used for filler passes. The joint underwent both non-destructive and destructive testing. Non-destructive and macroscopic tests classified the joint at quality level B. Microscopic examinations revealed a ferritic–austenitic microstructure with varying ferrite content in different joint areas. The joint exhibited high tensile strength (~790 ± 7 MPa), high ductility (weld metal: ~160 ± 4 J; HAZ: ~216 ± 26 J), and plasticity (180° bending with no macrocracks). Hardness did not exceed 280 HV10 across the joint cross-section [26].

The microstructure and pitting corrosion resistance of S32101 duplex stainless steel keyhole tungsten inert gas welded joints under different heat inputs were studied. Electrochemical experiments in a 1 mol/L NaCl solution at room temperature tested the pitting rupture potential of the heat-affected zone and weld metal zone. Results showed that increasing heat input led to more ferrite converting to austenite and an increase in the number and size of intragranular austenite grains in the weld metal zone. Austenite content increased in both the HAZ and weld metal zone with higher heat inputs. Chromium nitrides (CrN and Cr_2N) were mainly precipitated in ferrite, at austenite, and ferrite/austenite interfaces. Higher heat inputs increased the pitting rupture potential and pitting corrosion resistance of the HAZ and weld metal zone. The relationship between CrN and Cr_2N positions, austenite content, and pitting corrosion resistance was elucidated, revealing that the best pitting corrosion resistance was achieved with 2.46 kJ/mm heat input [27].

The effect of induction solution heat treatment using autogenous TIG welding on UNS S31803 DSS sheets was evaluated. Samples were treated at 1050 and 1150 °C for 10 seconds and compared to the as-welded condition. Quantitative and qualitative analyses, microstructural characterization using confocal microscopy, and corrosion resistance studies per ASTM G48 standard were conducted. The optimal treatment (10 s at 1150 °C) eliminated chromium nitrides and restored the ferrite-austenite phase balance. This treatment reduced hardness and produced welds free of cracks and discontinuities, with a low corrosion rate [28].

Pure argon gas was used in the inner layer, while a small amount of active gas was added to the outer layer during welding. The efficiencies and phase ratios in the weld microstructure of 2205 duplex stainless steel under different outer shielding gas conditions were compared. Different solution treatment conditions were applied post-welding to study their effect on weld microstructure. Experimental results showed that adding an appropriate amount of active gas to the outer protective gas improved welding efficiency. Proper solution treatment increased the austenite phase proportion in the welds. As the solution temperature and time increased, austenite content rose, grains became finer, and the phases were more uniformly distributed [29].

These studies collectively underscore the critical aspects of welding DSS, such as the importance of maintaining phase balance, controlling heat input, and managing cooling rates. The insights provided by these research efforts lay a solid foundation for exploring advanced welding techniques, such as the use of a toroidal nozzle, which could offer enhanced control over the welding environment and improve the quality of DSS welds.

The aim of the work was to demonstrate an increase in the durability and service life of welded joints produced using the patent solution in the form of a toroidal shielding gas nozzle compared to the durability and service life of welded joints made in duplex steels produced using the traditional TIG method.

MATERIALS AND METHODS

The material used for the construction of welded joints was 1.4462 (X2CrNiMoN22-5-3, AISI 2205) grade duplex steel of the chemical composition given in Table 1 (based on manufacturer's certificate).

The technological tests of welding were aimed at making a traditionally welded joint No. I (without the use of a toroidal shielding gas nozzle) and a welded joint No. II with the use of a toroidal shielding gas nozzle. The toroidal shielding was designed and constructed to improve the durability and service life of welded joints of the pipe with sheet metal.

Test welded joints of type I and II were made of the following materials:
- sheet metal with a thickness of 25 mm in 1.4462 grade steel according to PN-EN 10272:2016-09,

Table 1. Chemical composition of steel 1.4462, %wt. (based on manufacturer's certificate)

	C	Si	Mn	P	S	Cr	Ni	Mo	N	Cu
Sheet metal										
min	0.025	0.26	1.813	0.0287	0.0003	21.00	4.50	2.50	0.14	0.197
max	0.030	1.00	2.000	0.0300	0.0150	23.00	6.50	3.50	0.20	0.750
Pipe with a diameter of Ø25 × 2.5 mm										
	C	Si	Mn	P	S	Cr	Ni	Mo	N	
	0.029	0.48	1.55	0.023	0.003	22.30	4.60	3.18	0.160	
Pipe with a diameter of Ø38 × 1.6 mm										
	C	Si	Mn	P	S	Cr	Ni	Mo	N	
	0.027	0.48	1.74	0.024	0.002	22.40	5.19	3.30	0.190	

- pipe with a diameter of Ø25 × 2.5 mm made of grade 1.4462 steel according to PN-EN 10216-5:2021-09,
- pipe with a diameter of Ø38 × 1.6 mm made of grade 1.4462 steel according to PN-EN 10216-5:2021-09.

TIG welding in argon shielding was intended to join Ø25 × 2.5 mm (I, II) and Ø38 × 1.6 mm (I, II) diameter tubes to 25 mm thick sheet of ferritic-austenitic steel. The tests were carried out using the traditional TIG welding method and the TIG method with the application of tool in the form of a toroidal shielding gas nozzle. The nozzle is shown in Figure 1. The toroidal shielding gas nozzle is intended for orbital welding of tubes with sieve bottoms, especially for heat exchangers, using the method of welding with a non-melting tungsten electrode in the shielding of inert gases TIG, A-TIG for activated tungsten inert gas, or GTAW for gas tungsten arc welding such as argon, helium, or argon-helium mixtures. The purpose of the nozzle is to ensure continuous transmission of the shielding gas to the heated zone during the welding process, which is exposed to oxidation resulting from the high reactivity of the alloy elements with the atmospheric air during the process of welding high alloy-steels, titanium and its alloys. The advantage of the toroidal gas nozzle is the protection of the designated sites, which at the moment of welding are located in the vicinity of the non-melting electrode. The scope of work included executing:

- functional welding tests using the above nozzle,
- non-destructive and destructive tests in the designated scope,
- fatigue tests,
- evaluation of the results of the welded joints tests by an external scientific unit.
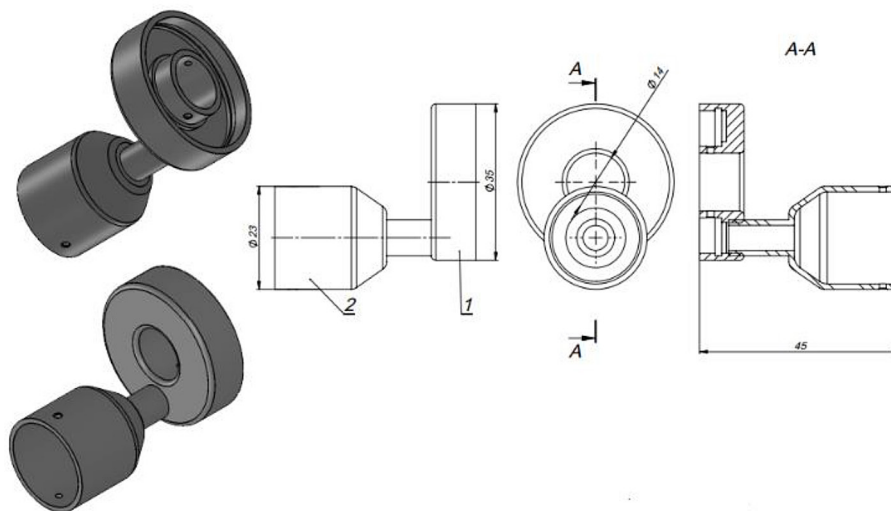
Figure 1. A toroidal shielding gas nozzle used for welding the pipe with a diameter of 25 mm,
1 – mounting pad; 2 – toroidal nozzle

The fixed structure of the test welded joints and the stitch in Welding Procedure Specification (WPS) is shown in the drawing in Figure 2. Welding process 142 was carried out in accordance with PN-EN ISO 4063. The Polysoude P6 (Head 8-75) was a welding source/tool. For making the joint No. I, butt weld with partial penetration (BW ½ V) was used. Tungsten electrode type WLa10 of 2.4 mm diameter, gas type, according to EN ISO 14175: I1-Ar was used. For welding variant No. I seventeen tests were performed and marked from 1–1 to 1–6 and from 3–1 to 3–11. Correspondingly, for welding variant No. II seventeen tests were performed and marked from 2–1 to 2–6 and from 4–1 to 4–11. Table 2 presents the conditions for making joints No. I and No. II.

RESEARCH RESULTS AND DISCUSSION

Non-destructive testing

Visual tests (VT)

Visual tests were carried out for the welded joints. The assessment was based on the PN-EN ISO 17637:2017-02 standard. No welding imperfections were found on the surface of the tested welded joints. The shape and dimensions of the weld met the specified requirements set out in the welding process manual. The results of visual tests for the above-mentioned joints met the quality level B in accordance with the standard PN-EN ISO 5817:2023-08 and no detected discontinuities according to PN-EN ISO 6520-1:2009. Figure 3 shows an example of a welded joint No. I (sample 1–1 and sample 3–4), and a welded joint No. II (sample 2–1 and sample 4–4). After a visual assessment and positive rating of the tested joints, they were approved for penetration tests.
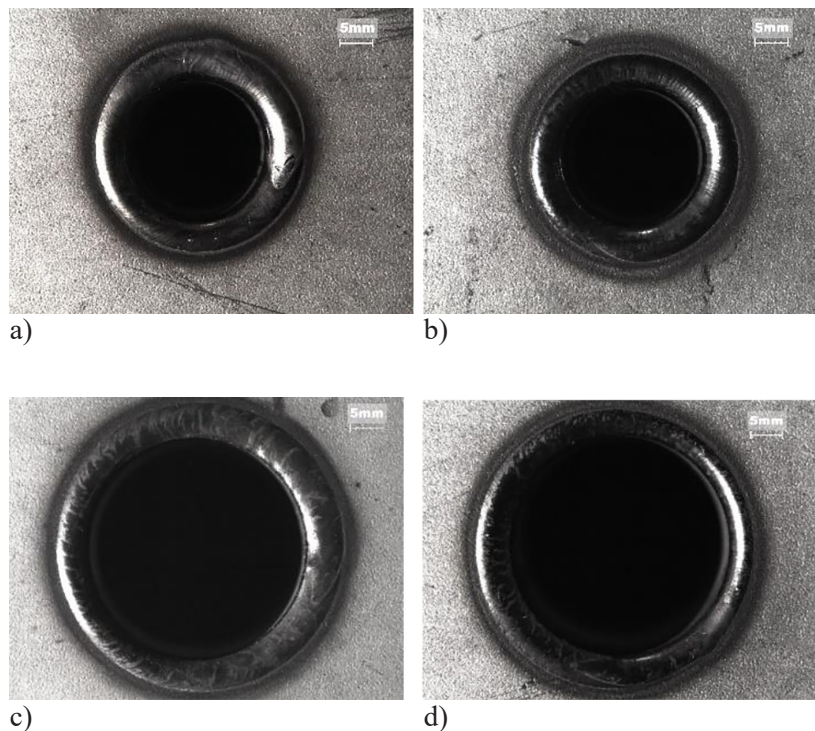
Penetration tests (PT)

At the next stage of testing welded joints, penetration tests were performed. The method of conducting the tests as well as their assessment were in accordance with the standard PN-EN ISO 3452-1:2021-12. A set of agents (remover, penetrant, developer) produced by the company Karl Deutsch was used to carry out penetration tests. The technique of carrying out individual operations was in accordance with Table 3. The results of PT for the above-mentioned joints met the acceptance level 2x according to PN-EN ISO
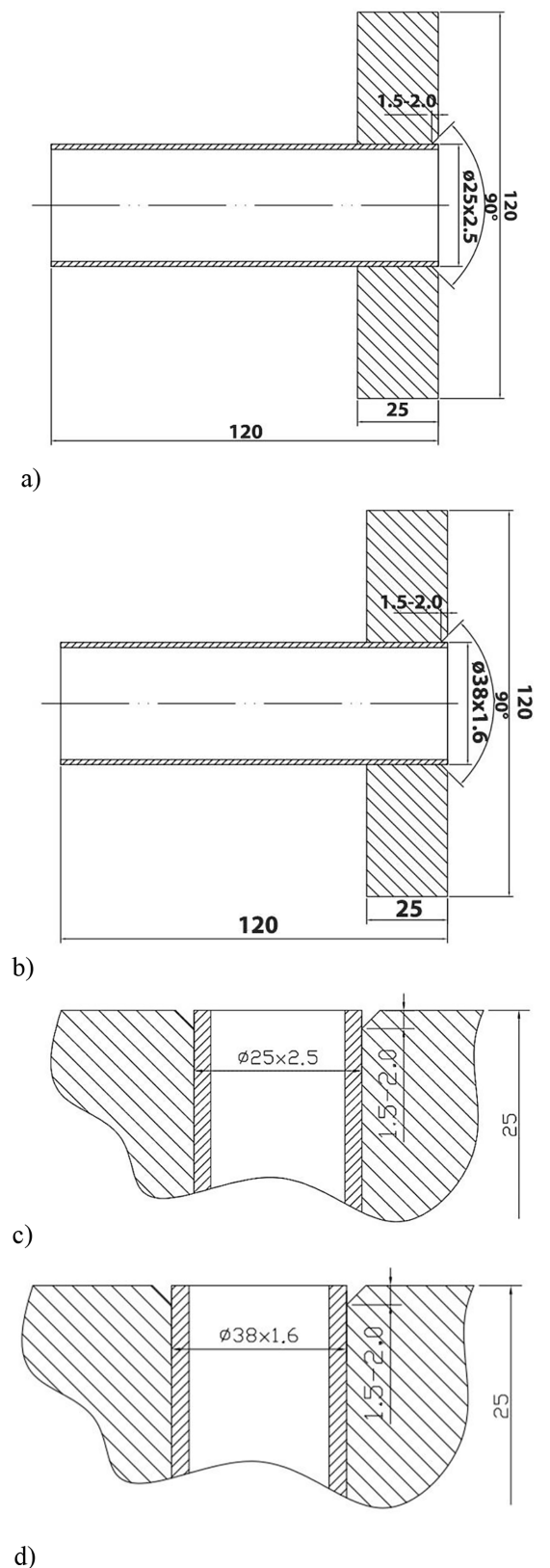
Figure 2. Welding sequences: (a) the structure of the welded test joint of duplex steel – pipe with a diameter of Ø25 × 2.5 mm, (b) the structure of the welded test joint of duplex steel – pipe with a diameter of Ø38 × 1.6 mm, (c) joint design the stitch in WPS Ø25 × 2.5 mm, (d) joint design the stitch in WPS Ø38 × 1.6 mm

Table 2. Welding parameters for the experiment No. I and No. II

Welding variant	Sample marking	Pipe diameter Ø, mm	Welding path, mm	Welding current I, A	Voltage U, V
I	1–1 ÷ 1–6	25	78.54	105	9
II	2–1 ÷ 2–6	25	78.54	80	9
I	3–1 ÷ 3–11	38	119.38	105	9
II	4–1 ÷ 4–11	38	119.38	80	9
Welding variant	Shielding gas flow (argon), l/min	Forming gas flow (argon), l/min	Total gas flow (argon), l/min	Q, heat input kJ/mm	Gas consumption for one joint, l
I	12	0	12	0.378	10.47
II	8	2	10	0.288	8.73
I	12	0	12	0.358	15.08
II	8	2	10	0.273	12.57

Figure 3. Example images of: (a) a traditionally welded joint No. I, sample 1–1, (b) a welded joint No. II with the use of a toroidal shielding gas nozzle, sample 2–1, (c) a traditionally welded joint No. I, sample 3–4, (d) a welded joint No. II with the use of a toroidal shielding gas nozzle, sample 4–4

23277:2015-05 guidelines. Quality level according to PN-EN ISO 5817:2023-08 was at level B. No welding imperfections were recorded for the tested joints. Following the next stage of testing, the joints were allowed to undergo volumetric - radiographic testing to detect internal imperfections.

Radiographic testing (RT)

Radiographic tests were carried out in accordance with PN-EN ISO 17636-1:2013-12. The radiographic tests carried out for the above-mentioned welded joints met acceptance level 1 according to PN-EN ISO 10675-1:2017-02 guidelines. Quality level according to PN-EN ISO 5817:2023-08 was at level B, no detected discontinuities according to PN-EN ISO 6520-1:2009. The observed optical density was in the range of 2.70 ÷ 2.82, and the quality image IQI was W14. After the non-destructive testing (NDT) the next stage was to select representative samples from each group and subject them to destructive testing (DT).

Table 3. Method of conducting penetration tests

Operation	Type of activity	Notes
1	Pre-cleaning	Manual
2	Degreasing and dehumidification	Manual
3	Penetrant application	Dwell time 15 min.
4	Washing and dehumidification	Manual
5	Application of the developer	Development time 25 min.
6	Inspection	After 15 and 30 min.
7	Cleaning and securing	Manual

Destructive testing of fabricated welded joints

Macroscopic examination

Macroscopic tests of welded joints were carried out in accordance with the following standards: PN-EN ISO 17639:2013-12, PN-EN ISO 15614-8:2016-06, and the assessment was carried out in accordance with the standard: PN-EN ISO 5817:2023-08. Macroscopic examinations were performed with a MOTIC type SMZ-168 stereo microscope equipped with a 3.0MP MOTICAM digital camera. As a result of the tests, it was found that the welds marked with numbers 1–1, 2–1, 3–4 and 4–4 were made appropriately, which are presented in Figure 4. It was found that the joints marked with numbers from 1–1 to 1–6 and from 2–1 to 2–6 were made correctly. Macroscopic examinations for samples 3–1, 3–2, 3–3 and 4–1, 4–2, 4–3 were classified negatively and rejected. Figure 4 shows an example of a properly welded joint No. I (sample 1–1 and sample 3–4), welded joint No. II (sample 2–1 and sample 4–4), negatively classified and rejected (sample 3–1). In Figure 4e) of the sample rejected (sample 3–1), an incomplete root penetration is visible. According to the standard PN-EN ISO 5817:2023-08, this type of defect is designated with the number (4021). This non-conformity pertains to single-sided butt welds, as was the case during the execution of this joint.

Ferrite content testing

The ferrite content was measured on the basis of the following standards: PN-EN ISO 17655:2003, PN-EN ISO 8249:2018-11 and test procedure No. PB-20. A portable ferritometer – Feritscope Fischer type MP30 serial number: SN030001950 with EGAB1.3-FE probe – was used for measurements. The ferrite content was measured in accordance with the markings applied in Figure 5. The ferrite content tested on the surface for the above-mentioned welded joints is in the range of 37.10% ÷ 63.77%. For traditionally welded samples, marked 1, the smallest ferrite content was in sample 1–2 BM (38.17%) and the largest (63.77%) in sample 1–4 WZ. For samples welded using a toroidal nozzle, marked 2, the smallest ferrite content was in sample 2–6 BM (37.67%) and the largest (60.42%) in sample 2–6 WZ. For traditionally welded samples, marked 3, the smallest ferrite content was in sample 3–11 BM (37.10%) and the largest (60.82%) in sample 3–8 WZ. For samples welded using a toroidal nozzle, marked 4, the smallest ferrite content was in sample 4–11 BM (38.28%) and the largest (54.25%) in sample 4–10 WZ. The smallest ferrite contents were observed, regardless of the welding variant and sample dimensions, always in the native material, while the largest ferrite contents always in WZ.

In light of all requirements and in accordance with the guidelines of the standard PN-EN ISO 8249: 2018–11 for welded joints, the ferrite content should remain in the range of 30.0% to 70.0%. For durability and corrosion resistance of duplex steels, it is advisable that the percentages of the individual phases be balanced or as close as possible. The most closely matched contents of both phase components in the welding zone were obtained for samples 1–6 (52.73% ferrite), 2–2 (51.05%), 4–6 (52.35%), and 4–11 (52.53%). The results were within the range of 51.05% to 52.95%. For the heat-affected zone (HAZ), the most balanced contents of ferrite and austenite were observed with ferrite content in the range of 41.70% to 44.60% for samples 1–6 (41.70%), 2–2 (42.73%), 3–6 (44.60%), and 4–10 (43.88%). In the welding zone, the most balanced ferrite content was 51.05%, whereas in the HAZ it was 44.60%.
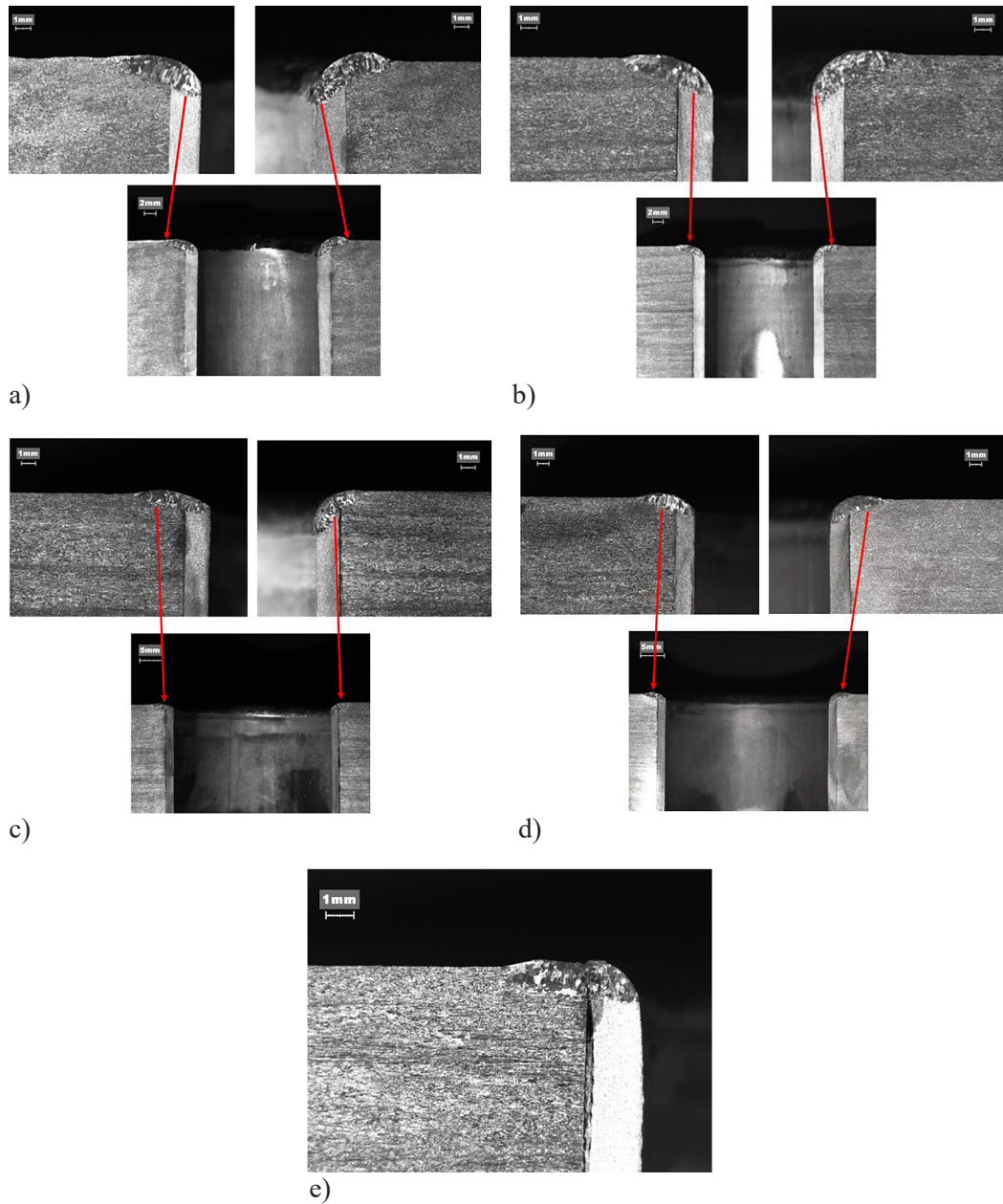
Figure 4. Example images of macroscopic examinations of: (a) sample 1–1, (b) sample 2–1, (c) sample 3–4, (d) sample 4–4, (e) rejected sample 3–1

Hardness testing

Macrohardness measurements were made with the HPO-250 hardness tester using the Vickers scale. The measurements were made in accordance with the standard PN EN ISO 6507-1: 2018-05. Imprints were made on the tested sample in accordance with the diagram shown in Figure 6.

The hardness results for the above-mentioned welded joints met the requirements of the standard PN-EN ISO 9015-1:2011. Summary of hardness measurement results, for example, for samples 1–1, 2–1, 3–4 and 4–4 are present in Table 4. The average hardness values in the individual zones for all samples did not exceed the permissible value of 380 HV10. For the samples presented in Table 4, depending on the zone, the average hardness value for sample 1–1 ranged from 238 to 316 HV10, for sample 2–1 it ranged from 238 to 283 HV10, for sample 3–4 it ranged from 238 to 321 HV10, and for sample 4–4 it ranged from 238 to 287 HV10.

The highest hardness for traditional TIG welding No. 1 was obtained at the boundary of the heat-affected zone (HAZ) and the welded pipes BM2: sample 1–1 (316 HV10) and sample 3–4 (321 HV10). For welded joint No. II with the

Figure 5. Places of measurement of the ferrite content in individual zones (BM – base material, HAZ – heat-affected zone, WZ – welding zone)
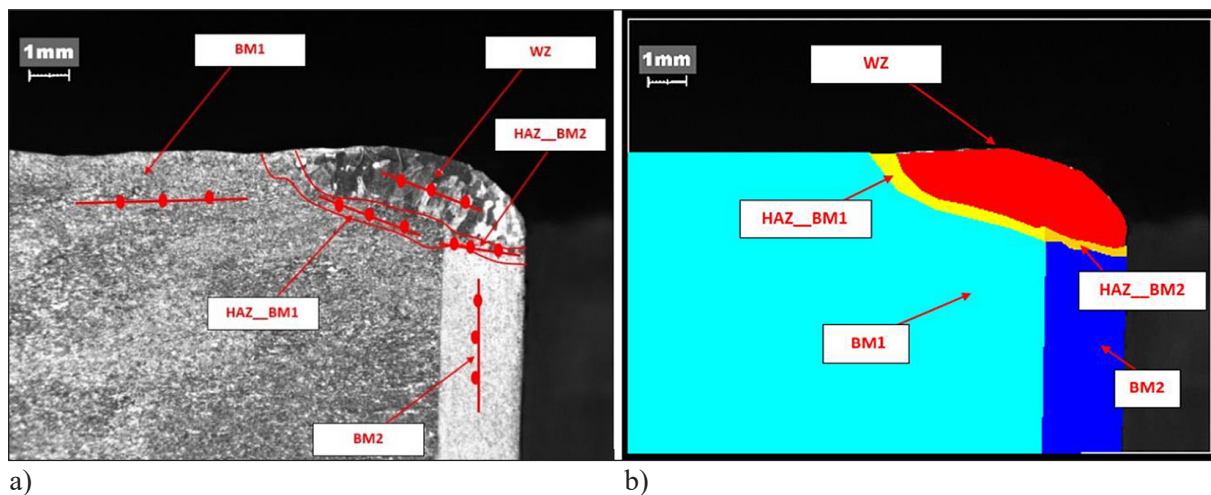
Figure 6. Measurements points of hardness measurement in individual zones: a) measurement method, b) aeras scheme

use of a toroidal shielding gas nozzle, the highest hardness values were in the welding zone (WZ): sample 2–1 (283 HV10) and sample 4–4 (287 HV10). Comparing the average hardness values in the HAZ_BM2, for traditional welding No. I, they are higher by almost 17% than for welding No. II with the use of a toroidal shielding gas nozzle for a pipe diameter of 25 mm, and 16% for a pipe diameter of 38 mm. Comparing the average hardness values in the WZ, for traditional welding No. I, they are lower by almost 5% than for welding No. II with the use of a toroidal shielding gas nozzle for a pipe diameter of 25 mm, and 6% for a pipe diameter of 38 mm.

Microscopic examination

In order to determine the microstructure, four transverse metallographic microsections were made – sampled from welds marked with numbers 1–1, 2–1, 3–4 and 4–4. For this purpose, the collected samples were embedded in DURACRYL acrylic resin and ground on water-proof abrasive papers of different grain size on a metallographic grinder. The samples prepared in this way were polished with diamond pastes and etched with Murakami reagent (100 ml of water, 10 g of $K_2Fe\,(CN)_6$, 10 g of KOH or NaOH). The prepared metallographic microsections were subjected to microscopic observation on an inverted metallographic microscope, the NIKON MA100 equipped with a Zeiss ERc-5s AxioCam digital camera. The microstructure of samples 1–1 and 2–1 are shown in Figure 7. The microstructure of samples 3–4 and 4–4 is shown in Figure 8.

Computer image analysis was performed on recorded images of microstructures using the NIS

Table 4. Summary of hardness measurement results for example, for samples 1–1, 2–1, 3–4 and 4–4

Sample	Average HV10
1-1 BM1	238
1-1 HAZ__BM1	304
1-1 WZ	269
1-1 HAZ__BM2	**316**
1-1 BM2	247
2-1 BM1	238
2-1 HAZ__BM1	267
2-1 WZ	**283**
2-1 HAZ__BM2	271
2-1 BM2	246
3-4 BM1	238
3-4 HAZ__BM1	296
3-4 WZ	271
3-4 HAZ__BM2	**321**
3-4 BM2	250
4-4 BM1	238
4-4 HAZ__BM1	267
4-4 WZ	**287**
4-4 HAZ__BM2	278
4-4 BM2	250

Note: BM1 – 25 mm thick sheet metal, BM2 – Ø25 pipe with a thickness of 2.5 mm for sample 1–1 and 2–1, BM2 – Ø38 pipe with a thickness of 1.5 mm for sample 3–4 and 4–4.

Elements 3.0 AR computer program. For identification, images from the NIKON MA100 metallographic microscope with 200x microscopic magnifications were used. Images of microstructures were subjected to binarization. Image calibration was performed with the recorded magnification in the microscopic image.

The analysis was performed only for a limited heat–affected zone (after rejecting the areas of the base material and weld). The width of the HAZ is 525px – which for the value of the calibrated scale (1 px = 0.31 µm) corresponds to 162.75 µm. The presented comparison of the limitation of the heat impact zone itself in the aspect of determining the phase share did not differ significantly. In the final analysis, the results for the entire recorded areas: BM1 (base material of the 25 mm thick sheets), HAZ_BM1, WZ, HAZ_BM2, BM2 (base material of the pipes) were calculated.

The percentage areas of the microstructure components were determined. The values of the percentage share of phase components for the analysed samples 1–1, 2–1, 3–4 and 4–4 determined

using computerized image analysis are presented in Table 5. For the entire analysed image in Figure 7g (sample 2–1), the percentage share of ferrite is 51.5% and for austenite it is 48.5%. For the heat–affected zone of the sample marked as 2–1 (Figure 7i), the percentage of ferrite is 51.2% and for austenite it is 48.8%. Comparable results of microstructure analysis were obtained for sample 4–4. For the weld zone (Figure 8h), the percentage share of ferrite is 48.6% and for austenite it is 51.4%. For the HAZ of the sample marked as 4–4 (Figure 8i), the percentage of ferrite is 51.4% and for austenite it is 48.6%. For the described samples, a greater phase balance in duplex steel welded joints is visible for welding No.II with a toroidal nozzle.

X-ray diffraction analysis

X-ray diffraction analysis was performed with DRON-1.5 diffractometer using X-ray tube radiation with a cobalt anode, filtered with iron. Recordings were made in the scope of 2 – theta angles from 48.0 to 126.0° in steps of 0.1°. The full measurement for the above-mentioned angular range was performed for the base material with a thickness of 6 mm and 8 mm. For the remaining samples, the measurement was performed in the angle range from 49.5 to 53.5° in steps of 0.1°. The voltage of the lamp was 35 kV, the amperage was 6 mA. A scintillation counter was used as a detector. A qualitative phase analysis was performed by comparing the obtained d_{hkl} interplanar distances and relative intensities with the ASTM catalogue data.

Figure 9a shows a diffractogram of the sample of the metal sheet of the base material with a thickness of 25 mm, and Figure 9b shows a diffractogram of the base material of the pipe with a diameter ø 25 × 2.6 mm. Figure 9c shows a diffractogram of the material of the pipe with a diameter of ø 38 × 1.6 mm.

Table 6 presents the results of phase identification for the base material of a pipe with a diameter of ø 25 × 2.6 mm, while Table 7 shows the results for a pipe with a diameter of ø 38 × 1.6 mm.

The two strongest lines were used to assess the content of the Fe_α (ferrite) and Fe_γ (austenite) phases. Therefore, the diffraction analyses were performed within the angle range from 49.5° to 53.5° in steps of 0.1°. Two of the strongest lines were analysed: {111} γ and {110} α. The share of austenite (V_γ) in the duplex steel matrix
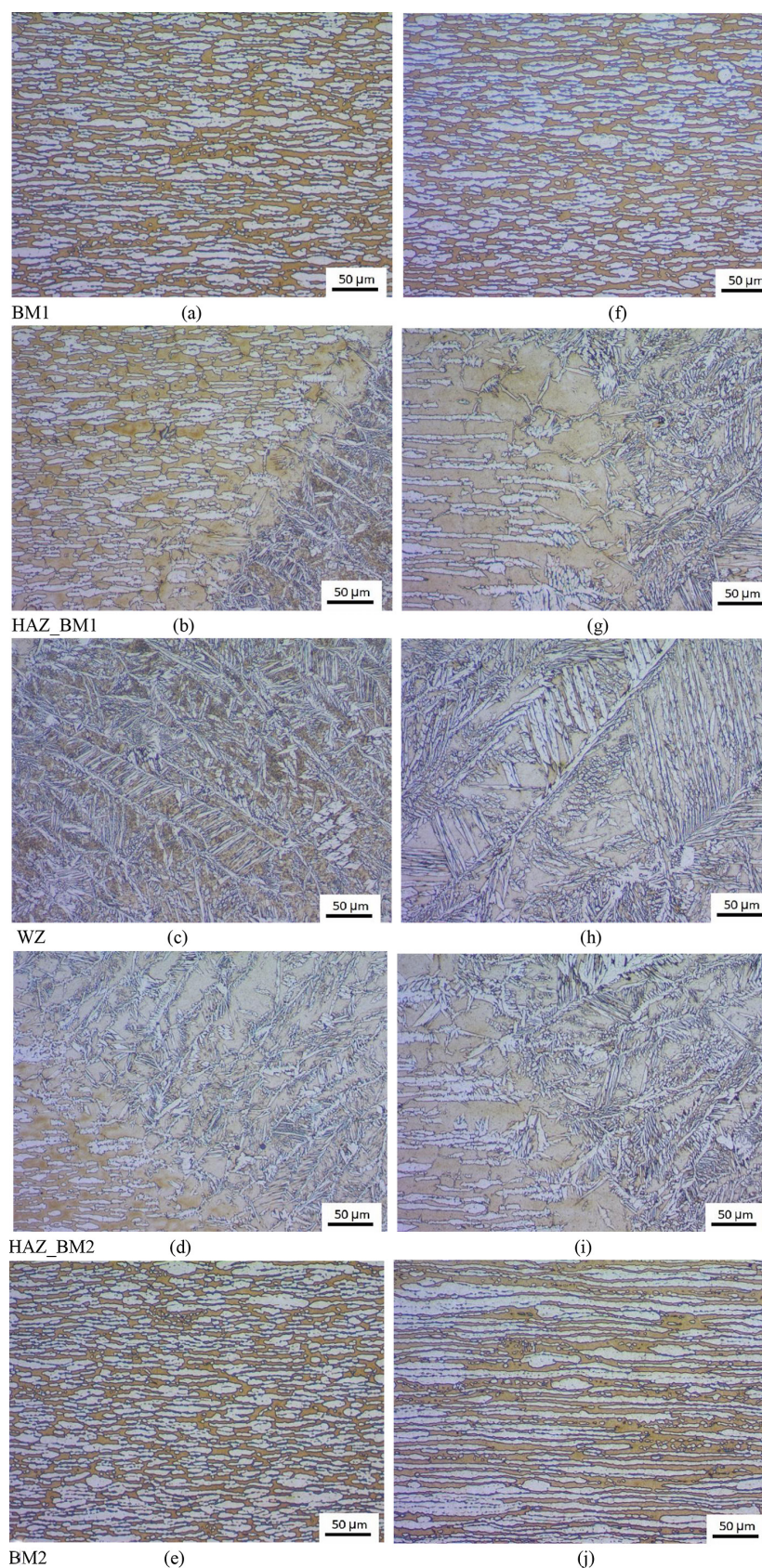
Figure 7. Light optical micrograph of austenitic microstructure (white fields) – ferritic (brown fields) duplex steel. Sample 1–1: Figures (a) ÷ (e). Sample 2–1: Figures (f) ÷ (j). Microscopic magnification 200x. BM1(a, f) – base material of the 25 mm thick sheets, HAZ_BM1 (b, g) – heat–affected zone adjacent to MR1, WZ (c, h) – visible crystallization front during weld cooling, HAZ_BM2 (d, i) – heat–affected zone adjacent to BM2, BM2 (e, j) – base material of the pipes with a diameter ø25 × 2.5 mm
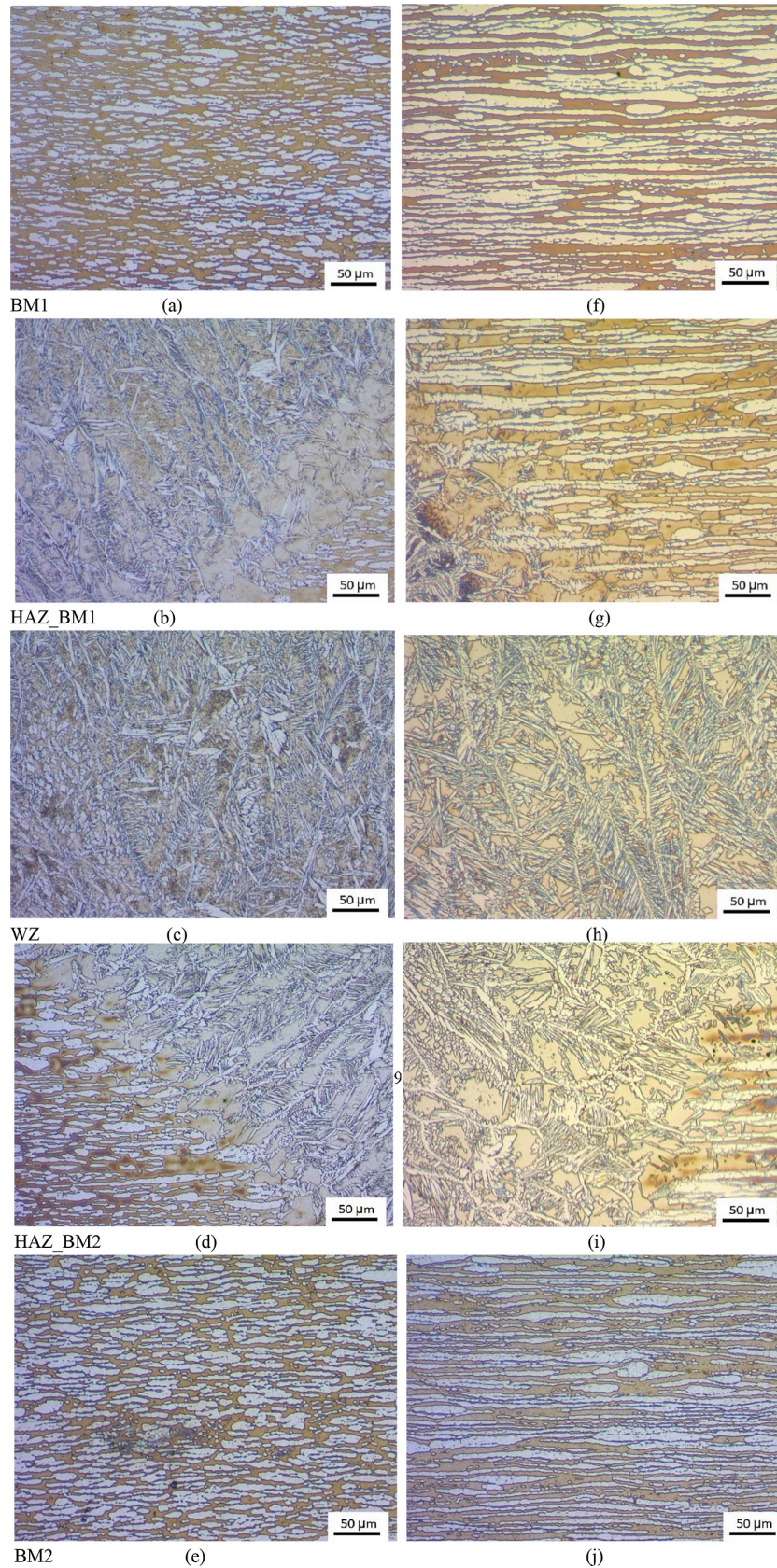
Figure 8. Light optical micrograph of austenitic microstructure (white fields) – ferritic (brown fields) duplex steel. Sample 3–4: Figures (a) ÷ (e). Sample 4–4: Figures (f) ÷ (j). BM1(a, f) – base material of the 25 mm thick sheets, HAZ_BM1 (b, g) – heat–affected zone adjacent to MR1, WZ (c, h) – visible crystallization front during weld cooling, HAZ_BM2 (d, i) – heat–affected zone adjacent to BM2, BM2 (e, j) – base material of the pipes with a diameter ø38 × 1.6 mm

**Table 5.** Values of the % share of phase components

Sample	BM1		HAZ_BM1		WZ		HAZ_BM2		BM2	
	V_g,%	V_α, %	V_γ,%	V_α, %	V_γ,%	V_α, %	V_γ,%	V_α, %	V_γ,%	V_α, %
1–1	58.6	41.4	69.1	30.9	40.3	59.7	68.7	31.3	54.2	45.8
	Figure 7a		Figure 7b		Figure 7c		Figure 7d		Figure 7e	
2–1	59.4	40.6	**48.5**	**51.5**	47.2	52.8	**51.2**	**48.8**	55.6	43.4
	Figure 7f		Figure 7g		Figure 7h		Figure 7i		Figure 7j	
3–4	57.3	42.7	69.5	30.5	42.2	57.8	67.9	32.1	53.9	46.1
	Figure 8a		Figure 8b		Figure 8c		Figure 8d		Figure 8e	
4–4	58.9	41.1	47.3	52.7	**48.6**	**51.4**	**51.4**	**48.6**	56.0	44.0
	Figure 8f		Figure 8g		Figure 8h		Figure 8i		Figure 8j	
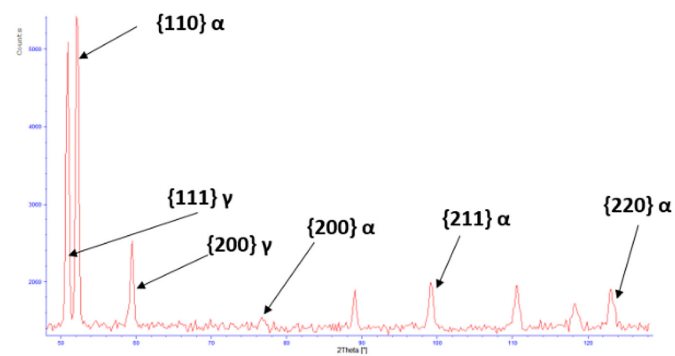
(a)
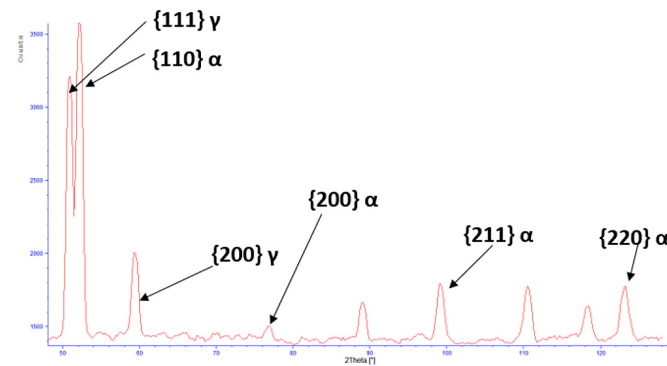
(b)
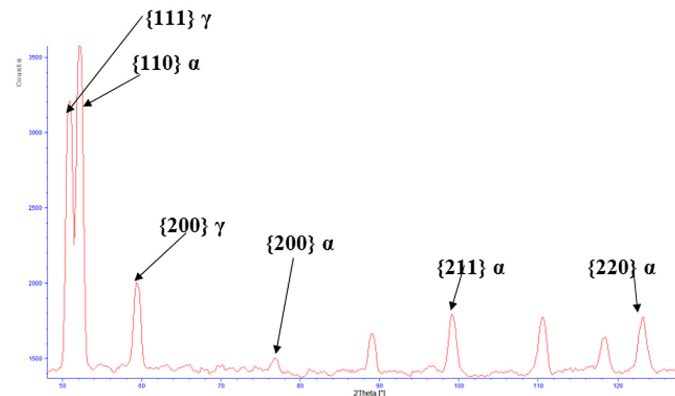
(c)

Figure 9. Diffractogram of the sheet metal base material: (a) with a thickness of 25 mm, (b) of the pipe with a diameter of ø 25 × 2.5 mm, (c) of the pipe with a diameter of ø 38 × 1.6 mm

Table 6. Phase identification results for the base material of the pipe with a diameter of ø 25 × 2.6 mm

Line no.	Diffraction data			ASTM catalog for Fe$_\gamma$			ASTM catalog for Fe$_\alpha$		
	d_{hkl}[1], Å	I[2], imp/s	I_{rel}[3], %	d_{hkl}, Å	I_{rel}, %	hkl	d_{hkl}, Å	I_{rel}, %	hkl
1	2.0819	1781	100.00	2.07	100.00	111			
2	2.0299	2144	100.00				2.0268	100.00	110
3	1.8084	563	31.61	1.80	50.00	200			
4	1.4386	71	3.31				1.4332	19.00	200
5	1.1755	362	16.88				1.1702	30.00	211
6	1.0164	345	16.09				1.0134	9.00	220

Note: d_{hkl}[1] – interplanar spacing, Å, I[2] – absolute intensity, imp/s, I_{rel}[3] – relative intensity, %.

(depending on the site of measurement) was determined from formula 1 [31, 32]:

$$V_\gamma = \frac{1}{1 + I_\alpha \cdot I_\gamma^{-1} \cdot R} \cdot 100 \ \% \quad (1)$$

where: V_γ – austenite content by volume, %; I_α – the total relative intensity of the phase diffraction line (110) α, planimetered on the roentgenogram, imp; γ – the total relative intensity of the phase diffraction line (111) γ, planimetered on the roentgenogram, imp; R – constant value adopted from the work [32] for these measurements 0.85.

$$V_\gamma + V_\alpha = 100 \ \% \quad (2)$$

The results for the phase composition of Fe$_\alpha$ (ferrite) and Fe$_\gamma$ (austenite) determined by the X-ray diffraction method according to Equations 1 and 2 for the analyzed joints, labelled 1–1, 2–1, 3–4, and 4–4, are presented in Table 8.

For the phase composition of austenite and ferrite in welded joints determined by X-ray diffraction (Table 8), a greater phase balance in duplex steel welded joints is observed for welding No. II with a toroidal nozzle. In the weld zone (WZ), the ferrite volume ranges from 48.62% to 60.06%, while in the heat–affected zone of base metal (HAZ_BM2) it ranges from 34.77% to 50.95%. In the weld zone for sample 2–1, the percentage of ferrite is 51.06% and austenite is 48.94%; for sample 4–4, the percentage of ferrite is 48.62% and austenite is 51.38%. Similar results were obtained in HAZ_BM2. For sample 2–1, the percentage of ferrite is 48.9% and austenite is 51.1%. For

Table 7. Phase identification results for the base material of the pipe with a diameter of ø 38 × 1.6 mm

Line no.	Diffraction data			ASTM catalog for Fe$_\gamma$			ASTM catalog for Fe$_\alpha$		
	d_{hkl}[1], Å	I[2], imp/s	I_{rel}[3], %	d_{hkl}, Å	I_{rel}, %	hkl	d_{hkl}, Å	I_{rel}, %	hkl
1	2.0817	1814	100.00	2.07	100.00	111			
2	2.0297	2157	100.00				2.0268	100.00	110
3	1.8088	571	31.48	1.80	50.00	200			
4	1.4379	76	3.52				1.4332	19.00	200
5	1.1748	375	17.39				1.1702	30.00	211
6	1.0169	352	16.32				1.0134	9.00	220

Table 8. Phase composition of austenite and ferrite in welded joints determined by X-Ray diffraction method

Parameter	Analyzed area									
	BM1		HAZ_BM1		WZ		HAZ_BM2		BM2	
Sample	V_γ,%	V_α, %	V_γ,%	V_α, %	V_γ,%	V_α, %	V_γ,%	V_α, %	V_γ,%	V_α, %
1–1	60.88	39.12	66.75	33.25	37.94	62.06	65.23	34.77	53.83	46.17
2–1	60.95	39.05	45.81	54.19	**48.94**	**51.06**	**51.10**	**48.90**	52.79	47.21
3–4	61.47	38.53	64.89	35.11	40.46	59.54	64.71	35.29	51.18	48.82
4–4	61.13	38.87	47.13	52.87	**51.38**	**48.62**	**49.05**	**50.95**	53.10	46.90

sample 4–4, the percentage of ferrite is 50.95% and austenite is 49.05%. The phase balance in these duplex steel welded joints is therefore very close to 50:50. According to the literature [12, 13], a 50:50 balance of ferrite to austenite achieves the best corrosion resistance and mechanical properties in DSS weldments.

The obtained results show a better phase balance compared to the study [24], where the ferrite volume fraction in the ATIG weld zone was 54% and in the TIG weld zone was 47%.

Fatigue tests (scope and results)

Static resistance tests – all the tests were performed with the INSTRON 8502 hydraulic testing machine equipped with a servo cylinder allowing for application of loads in the range of ± 250 kN. Loading was applied from the top through the pin centring the sample against the axis of the testing machine and from the bottom through the support plates, symmetrically distanced from the machine. The samples were subjected to an increasing load with a piston travel speed of 0.02 mm/s. All samples cracked in the weld. The results of fatigue tests are presented in Table 9.

Static strength tests were performed to determine the value of the maximum force destroying

a welded joint. The value of the force (Table 9) which was determined served to prepare a load program in fatigue tests. Figure 10a shows static load graphs of the tested samples and Figure 10b – the results of sample fatigue tests. The value of the average destructive force for samples 1–2 and 2–1 was 72.9 kN and 74.8 kN, respectively, i.e. the average 73.8 kN.

Figure 11a shows static load graphs of the tested samples and Figure 11b – the results of sample fatigue tests. The value of the average destructive force for samples 3–4 and 4–4 was 81.5 kN and 80.3 kN, respectively, i.e. the average 80.9 kN.

The average destructive force for samples with a pipe diameter of Ø38 was almost 10% greater than for samples with a pipe diameter of Ø25. Fatigue tests – fatigue tests consisted in subjecting samples to variable zero-pulsating compression. The tests were performed on several levels in relation to the percentage of the destructive force value. The values of individual levels were 10%, 20%, 30%, 50%, 70%, respectively. The load frequency f was 6 Hz. Figure 10b and Figure 11b summarizes the values of the n fracturing cycles for individual samples, the levels of loading application F_{max} in the form of graphs. The obtained results were

Table 9. Fatigue test results

| No	Sample	Load level	Force *Fmax*, kN	Number of cycles, *n*
1	1–3	0.1	7.38	1402494
2	1–4	0.1	7.38	783454
3	1–6	0.2	14.76	138371
4	1–5	0.3	22.14	34916
5	2–3	0.1	7.38	3812073
6	2–4	0.1	7.38	1161785
7	2–6	0.2	14.76	157109
8	2–5	0.3	22.14	47685
9	3–9	0.1	8.09	1809721
10	3–10	0.1	8.09	1144248
11	3–11	0.2	16.18	265921
12	3–8	0.3	24.27	91820
13	3–7	0.5	40.45	19383
14	3–6	0.7	56.63	5686
15	4–8	0.1	8.09	1406903
16	4–9	0.1	8.09	3901099
17	4–7	0.2	16.18	277767
18	4–6	0.3	24.27	96133
19	4–10	0.5	40.45	21752
20	4–11	0.7	56.63	7895
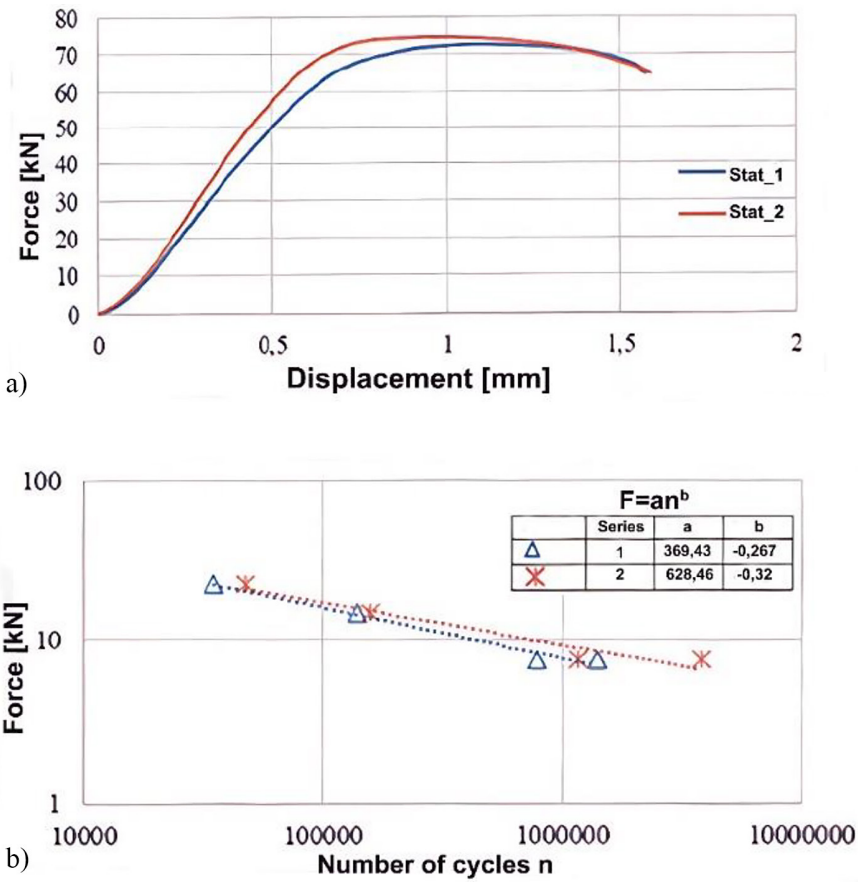
Figure 10. (a) Waveform diagrams of the loading of samples 1–1 and 2–1, (b) the results of sample fatigue tests
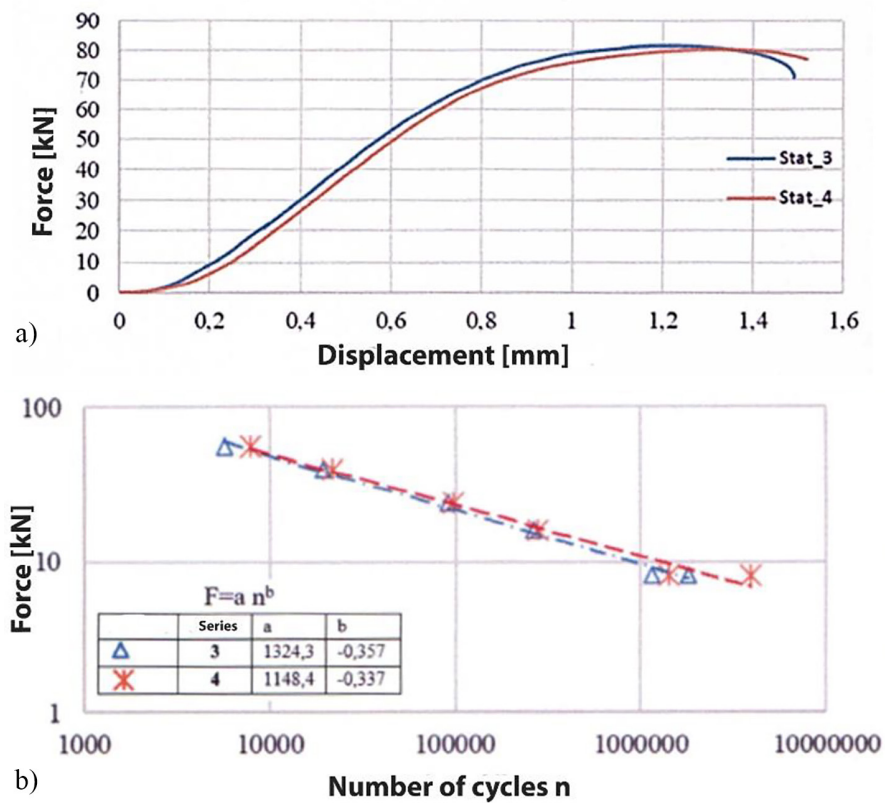

Figure 11. (a) Waveform diagrams of the loading of samples 3–4 and 4–4, (b) the results of sample fatigue tests

approximated with a regression equation in the form of $\log\sigma\_a = a\,\log N + b$.

In Figure 10b and Figure 11b, it can be observed that the fatigue curves intersect in the area of the high values of load forces F_{max}. This indicates the impact of the load level on the obtained durability. It is small at the highest levels and increases with the decrease of the load level. As the load level decreases, the spread of the obtained durability values also increases. Therefore, a larger number of samples tested at one load level is necessary for the quantitative assessment of the stability at these load levels.

The comparative analysis of the results for samples $1–3 \div 1–6$ and $2–3 \div 2–6$ as well as $3–6 \div 3–11$ and $4–6 \div 4–11$ shows a differentiation in the obtained durability. The fatigue charts made for traditional welding and with a toroidal nozzle intersect in the range of large load forces F_{max}. This indicates the influence of the load level on the obtained durability. It is small at the highest implemented load levels and increases as it decreases. Along with the decrease in the load level, the scatter of the obtained durability also increases. Therefore, to quantitatively assess the durability at these load levels, a larger number of samples tested at one load level is necessary.

Recapitulation

The results obtained from testing welded joints of two-phase duplex stainless steel 1.4462 using two methods: the classic TIG one and the TIG method using a toroidal shielding gas nozzle were analysed.

In the case of welding joints with the TIG classical method, in each of the examined cases, the share of ferrite in the weld by volume was higher by approximately 10% compared to the joints welded with the use of a toroidal nozzle (Table 5, Table 8). Increased ferrite content for the joints welded with No. I, in the case of exploitation, may result in lower corrosion resistance. A very similar content of ferrite and austenite was obtained only for welding No. II with a toroidal nozzle. For a pipe diameter of ø25 mm (sample 2–1), these were the HAZ_BM1 and HAZ_BM2 areas, and for a pipe diameter of ø38 mm, these were the WZ and HAZ_BM2 areas.

By analysing the durability determined on the basis of fatigue tests, it can be unequivocally stated that the welding No. II achieves better results. Depending on the variant of the combination and the level of load, this increase ranges from 4% to 132% (based on expert opinion from the Lodz University of Technology – may 2020).

For each joint type, there is a reduction in gas consumption by 17% when welding with a nozzle compared to conventional welding (based on expert opinion from the AGH University – 22.06.2020).

In the conducted studies, pure Ar was used as the shielding gas for TIG welding. Literature [10–12, 21] reports that favorable welding results are obtained when argon is combined with nitrogen or Ar gas with 0.4% O_2 [30]. It seems interesting to explore the application of gas mixtures in future studies.

CONCLUSIONS

Analysis of the results allows the following conclusions to be formulated:

- conventional welding, compared to welding using a toroidal nozzle, causes large differences in the microstructure of the welded joint in individual zones (HAZ, HAZ-BM);
- welding with the use of a toroidal nozzle reduces the amount of ferrite in the surface layers of the weld (HAZ-BM) and the HAZ, this form of things in the later operation of objects made in this way may translate into increased service life (through greater corrosion resistance);
- the tested welded joints in terms of the morphology of the phases: ferrite (α) and austenite (γ) differ significantly in the arrangement of individual phases – it is also varied (when using a toroidal nozzle) – even arrangement of one and the other phase, while in the case of classical welding, the share of ferrite (α) is definitely greater at the contact with the weld, while austenite (γ) is mainly concentrated at the base material (BM) (Figure 7 and Figure 8);
- the morphological distribution of the microstructure in welded joints for individual welding variants is confirmed by the results of hardness measurements;
- in the aspect of service life, as a result of dynamic objects, exchangers (tube sheets) are subjected to such conditions – values almost twice as high are obtained for a welded joint with the use of a toroidal nozzle.

REFERENCES

1. Francis R., Byrne G. Duplex stainless steels – Alloys for the 21st century. Metals 2021, 11(5), 836. https://doi.org/10.3390/met11050836

2. Kazakov A., Zhitenev A., Fedorov, Fomina O.V. Development of duplex stainless steels compositions. CIS Iron Steel Rev 2019, 18, 20–26. https://doi.org/10.17580/cisisr.2019.02.04

3. Łabanowski J. Stale Odporne na Korozję i ich Spawalność. Wydawnictwo Politechniki Gdańskiej, 2021.

4. Gunn R.N. Duplex Stainless Steels: Microstructure, Properties and Applications. Woodhead Publishing, 1997.

5. Brytan Z., Niagaj J. Corrosion resistance and mechanical properties of TIG and A-TIG welded joints of lean duplex stainless steel S82441/1.4662. Arch Metall Mater 2016, 61(2), 771–784. https://doi.org/10.1515/amm-2016-0131

6. Trydell K., Persson K., Fuertes N., Siewert E., Hussary N.,Pfreuntner., BengtssonP., JaniakP., VishnuR., Frodigh M. Ferrite fraction in duplex stainless steel welded with a novel plasma arc torch. Weld World 2023, 67, 805−817.

7. Francis R., Byrne G. The erosion corrosion limits of duplex stainless steels. Mater Performance 2018, 57(5), 44–47.

8. Francis R. The corrosion of duplex stainless steels: a practical guide for engineers. NACE International, Houston, TX, USA, 2018.

9. Łabanowski J., Świerczyńska A., Topolska S., Effect of microstructure on mechanical properties and corrosion resistance of 2205 duplex stainless steel. Pol. Marit. Res. 2014, 21(4), 108–112.

10. Hosseini V.A., Wessman S., Hurtig K., Karlsson L. Nitrogen loss and effects on microstructure in multipass TIG welding of a super duplex stainless steel. Mater Design 2016, 98, 88–97. https://doi.org/10.1016/j.matdes.2016.03.011

11. Lai R., Cai Y., Wu Y., Li F., Hua X. Influence of absorbed nitrogen on microstructure and corrosion resistance of 2205 duplex stainless steel joint processed by fiber laser welding. J Mater Process Tech 2016, 231, 397–405. https://doi.org/10.1016/j.jmatprotec.2016.01.016

12. Messer B., Oprea A., Wright A. Duplex stainless-steel welding: best practices. Stainl. Steel World 2007, 11, 53–63.

13. Karlsson L. Welding duplex and super duplex stainless steels. Anti-corros Meth Mater 1995, 42(6), 30–35. https://doi.org/10.1108/eb007380

14. Hosseini V.A., Hurtig K., Eyzop D., Östberg A., Janiak P., Karlsson L. Ferrite content measurement in super duplex stainless steel welds. Weld World 2018, 63(2), 551–563. https://doi.org/10.1007/s40194-018-00681-1

15. Dobra´nszky J., Ginsztler J. Microstructural stability of duplex stainless steel weldments. Mater. Sci. Forum 2007, 561–565, 2119–2122. https://doi.org/10.4028/www.scientific.net/MSF.561-565.2119

16. Karlsson L., Tolling J. Experiences and new possibilities in welding duplex stainless steels. In: IIW Regional Congress Welding and Related Inspection Technology for the Development of Southern Africa, Stellenbosch, South Africa, 8–10 March 2006.

17. Wang H.-S. Effect of welding variables on cooling rate and pitting corrosion resistance in super duplex stainless weldments. Mater Trans 2005, 46(3), 593–601. https://doi.org/10.2320/matertrans.46.593

18. Paulraj P., Garg R. Effect of intermetallic phases on corrosion behavior and mechanical properties of duplex stainless steel and super-duplex stainless steel. Adv. Sci. Technol. Res. J. 2015, 9(27), 87–105. https://doi.org/10.12913/22998624/59090

19. Aiguo L. Progress in weldability research of duplex stainless steels. China Weld. 2024, 33(2), 50–62. https://doi.org/10.12073/j.cw.20230806001

20. Ramesh A., Kumar V., Anuj, Khanna P. Weldability of duplex stainless steels – A review. E3S Web of Conferences 2021, 309, 01076. https://doi.org/10.1051/e3sconf/202130901076

21. Zhang Y., Liu Z., Jin M., Song S. Effects of nitrogen element on microstructure and pitting corrosion resistance of duplex stainless steel welded joints. Mater. Res. Express 2021, 8, 026514.1−026514.9.

22. Cui S., Yu Y., Tian F., Pang S. Morphology, microstructure, and mechanical properties of S32101 duplex stainless-steel joints in K-TIG welding. Materials, 2022, 15, 5432.1−5432.14.

23. Han L., Han T., Chen G., Bangyu W., Sun J., Wang Y. Influence of heat input on microstructure, hardness and pitting corrosion of weld metal in duplex stainless steel welded by keyhole-TIG. Mater Charact 2021, 175, 111052.1−111052.15.

24. Touileb K., Hedhibi A.C., Djoudjou R., Ouis A., Bensalama A., Ibrahim A., Abdo H.S., Ahmed M.M.Z. Mechanical, microstructure, and corrosion characterization of dissimilar austenitic 316L and duplex 2205 stainless-steel ATIG welded joints. Materials 2022, 15(7), 2470.1−2470.21.

25. Moonngam S., Wangjina P., Viyanit E., Banjongprasert C. Characterizing oxide inclusions in welded lean duplex stainless steels and their influence on impact toughness. Materials 2023, 16:1921.1−1921.10.

26. Krawczyk R., Słania J., Golański G., Pfeifer T. Mechanical properties and microstructure of austenite−ferrite duplex stainless steel hybrid (laser + GMAW) and SAW welded joint. Materials 2023, 16, 2909.1−2909.10.

27. Cui S., Pang S., Pang D., Tian F., Yu Y. The microstructure and pitting corrosion behavior of K-TIG welded joints of the UNS S32101 duplex stainless steel. Metals 2022, 16(1), 250.1−250.10.

28. Ai J., Hu Y., Wang H., et al. Research progress on corrosion of duplex stainless steel and its welded joint. Surface Technology 2022, 51(4), 77 − 91.

29. Ferreira P.M., Pereira E.C., Pinheiro F.W., Monteiro S.N., Azevedo A.R.G. Effect of solution heat treatment by induction on UNS S31803 duplex stainless steel joints welded with the autogenous TIG process. Metals 2022, 12, 1450.1−1450.13.

30. Zou Y., Zeng Q., Li L., Yunrui M. Effect of solution treatment on duplex stainless steel weld microstructure of deep-penetration TIG welding. Journal of Physics: Conference Series 2022, 2321, 012013.1−012013.5.

31. Senczyk D. Microstructural X-ray laboratory. Wydawnictwo Uczelniane Politechniki Poznańskiej, 1974. (in Polish).

32. Cullity B.D., Kołakowski B., Lefeld-Sosnowska M., et al. Fundamentals of X-ray diffraction. Warszawa, Państwowe Wydawnictwo Naukowe, 1964. (in Polish).